

Fluctuations in the CMB Induced by Cosmic Strings: Methods and Formalism

M. Landriau* and E.P.S. Shellard†

*Department of Applied Mathematics and Theoretical Physics
Centre for Mathematical Sciences,
University of Cambridge*

Wilberforce Road, Cambridge CB3 0WA, U.K.

(Dated: January 20, 2003)

We present methods to compute maps of CMB fluctuations from high resolution cosmic string networks using a full Boltzmann code, on both large and small angular scales. The accuracy and efficiency of these methods are discussed.

PACS numbers: 98.80.-k, 98.80.Cq

I. INTRODUCTION

The potential role of cosmic strings and other topological defects in cosmology has been the subject of considerable interest for well over two decades (for a review see ref. [1]). Perhaps the most exciting prospect would be the detection of their distinct observational signatures in the cosmic microwave sky. Cosmic strings, for example, are expected to create line-like discontinuities in the CMB temperature pattern, whereas other defects such as global monopoles or textures create ‘hot spots’. Their discovery would provide unprecedented information about the nature of unification in the early universe, while their absence from the CMB would significantly strengthen constraints on a wide range of models.

To many, the publication of the BOOMERanG results [2], in particular, signaled the demise of topological defects in cosmology. Indeed, the detection of an acoustic peak around $\ell \simeq 200$ was seen as evidence that primordial adiabatic perturbations were the seeds for large-scale structure formation, a view that has been strengthened with the apparent resolution of further peaks (see also [3, 4, 5]). However, the presence of defects is not incompatible with inflation and post-BOOMERanG analyses, such as refs. [6, 7], concluded that they could not be ruled out. Current data allows defects to play a significant (but subdominant) role in large-scale structure formation. In this sense, it is of great importance to accurately characterize nonGaussian signals from strings, as they are likely to provide the only direct method of detection.

In this paper we will detail the methods that we have developed to create full-sky and high resolution CMB maps generated by cosmic defects or any other ‘causal’ or ‘active’ sources. First, in §II we detail the large set of perturbation equations that have to be solved, following this in §III with a discussion of the treatment of the source terms which distinguish this analysis from that for inflationary fluctuations. In §IV we then discuss efficient numerical implementation of CMB map-making using the analogue of Green’s function techniques, without which the problem would not be tractable computationally. However, we complete this introduction by discussing previous work on cosmic defects and the CMB, pointing out its relationship to this paper.

Some of the earliest work featured analytic results obtained for simple string configurations [8, 9, 10]. Such exact solutions are important for testing computational methods. However, although these analytic results are interesting, numerical simulations are essential to obtain accurate quantitative predictions in more general contexts. The main drawback of numerical results in this context is their limited dynamic range, restricted by the light-crossing times of cosmic defect simulations. All-sky (large angle) CMB maps can be generated and have been used to obtain the normalization of the power spectrum to COBE, but their angular resolution has been poor. On the other hand, small angle maps permit the very important characterization of nonGaussian signals due to defects. Given the prospect of high resolution all-sky observations from the MAP and Planck satellites, ideally one would aim to compute all-sky defect maps of corresponding resolution, but computational resources remain insufficient for this task at present.

Probably the earliest attempt at computing realistic CMB patterns generated by defects was that of Bouchet, Bennett & Stebbins [11]. They employed a flat-space formalism to calculate the CMB temperature $\Delta T/T$ in the

*Current address: Laboratoire de l’Accélérateur Linéaire, IN2P3-CNRS et Université Paris-Sud, B.P. 34, 91898 Orsay Cedex, France.;
Electronic address: landriau@lal.in2p3.fr

†Electronic address: E.P.S.Shellard@damtp.cam.ac.uk

direction $\hat{\mathbf{n}}$, solving the metric perturbation equations using Green's functions $G(\mathbf{k}, t, t')$ schematically as:

$$\frac{\Delta T}{T}(\hat{\mathbf{n}}, \mathbf{k}, t) \propto \int G_{\mu\nu}(\hat{\mathbf{n}}, \mathbf{k}, t, t') \Theta_{\mu\nu}(\mathbf{k}, t') dt', \quad (1)$$

where $\Theta_{\mu\nu}$ is the energy-momentum tensor of cosmic strings. Their methods neglected many effects, notably the presence of baryons and the expansion of the Universe, concentrating solely on the integrated Sachs-Wolfe effect. Pen, Spergel & Turok [12] computed all-sky maps (at COBE resolution) produced by different global defects including an approximate treatment of CDM, baryons and radiation and their work was extended on intermediate angular scales in ref. [13]. COBE resolution maps generated by local cosmic strings were presented in [14] using the Allen-Shellard (AS) string code [15]. The power spectrum for this map was evaluated for $\ell \leq 20$ (using an ensemble of 192 realisations) and they inferred the string linear energy density to be $G\mu/c^2 = 1.05_{-0.20}^{+0.35} \times 10^{-6}$.

The most recent work on CMB fluctuations in the presence of causal seeds have made use of full Boltzmann codes (see section II), thus including all the relevant physics (to first order). The AS string code was employed again in the full Boltzmann analysis in ref. [16], in which power spectra were computed from the brightness distribution, thus bypassing the maps. Power spectra were computed from simulations of different cosmological epochs and provided clear evidence of the importance of vector and tensor modes in these models, as well as the apparent absence of strongly defined acoustic peaks.

An alternative line-of-sight approach was used in ref. [17], and also later in refs. [18, 19], to calculate power spectra for global defects. Here, the idea was to use unequal time correlators (UETCs) of the defect energy-momentum tensor (approximated by an expansion in eigenvectors) as the source for the perturbation power spectra. In principle, the method greatly extends the available dynamic range by exploiting the scalability of the correlators during defect evolution. However, while scalability is approached asymptotically in the radiation and matter eras, during the important radiation-matter transition the UETCs must still be calculated from large simulations bridging this time period. The line-of-sight method has also been used by [20, 21] who employed an ensemble of toy model realisations of a string network and averaged the power spectra. The line-of-sight method can be used to compute maps as well: Simatos & Periviaropoulos [22] modified it using a more general expansion of plane waves to accommodate for phase differences in a toy model for wiggly strings. However, while the method is phenomenologically interesting it was necessary to make a number of assumptions about the string perturbation phases.

It is important to note that none of these methods is perfect, and in some sense, they are complimentary: The direct approach developed further here, solving the full Boltzmann equations on a three-dimensional grid, provides reliable high resolution CMB maps. However, the UETC method with a greater dynamic range provides a more extensive view of the angular power spectrum.

II. COSMOLOGICAL PERTURBATIONS

In this section, we shall derive the equations that describe the evolution of first order perturbations in the metric and the energy-momentum tensor of matter fields in the presence of causal seeds such as cosmic strings. The formalism used is similar to that of [12], except here, the full Boltzmann equation for relativistic matter (photons, neutrinos) is used. The treatment of the Boltzmann distributions presented here follows on from the approach used for scalar modes by [23], but is extended to vector and tensor modes. The treatment of photon polarization follows the approach used by [24] for scalar and tensor modes, but is extended to vector modes. Similar, though not as general, methods were used by [18], where scalar and vector modes were treated in a gauge invariant formalism.

A. Scalar - Vector - Tensor Decomposition

In this paper, we will restrict ourselves to flat FRW models because present cosmic defect simulations are restricted to these. However, this is a significant simplification which enables us to expand all perturbations in terms of Fourier modes. In Fourier space, a tensor quantity T_{ij} can be decomposed into scalar T, T^S , vector T_i^V and tensor components T_{ij}^T in the following way:

$$T_{ij}(\mathbf{k}) = \frac{1}{3}\delta_{ij}T + (\hat{k}_i\hat{k}_i - \frac{1}{3}\delta_{ij})T^S + (\hat{k}_iT_j^V + \hat{k}_jT_i^V) + T_{ij}^T. \quad (2)$$

This is analogous to the manner in which vector quantities can be decomposed into scalar and vector components:

$$V_i(\mathbf{k}) = \hat{k}_iV^S + V_i^V. \quad (3)$$

In the above, vector and tensor components are tranverse that is, $\hat{k}_i V_i^V = \hat{k}_i T_i^V = \hat{k}_i \hat{k}_j T_{ij}^T = 0$ and tensor components are, in addition, traceless $T_i^T i = 0$. It is also useful to express vector components in an orthonormal basis $\mathbf{e}_1, \mathbf{e}_2$ with $\mathbf{e}_1 \times \mathbf{e}_2 = \hat{\mathbf{k}}$, so that

$$\mathbf{V} = V^S \hat{\mathbf{k}} + V_1^V \mathbf{e}_1 + V_2^V \mathbf{e}_2. \quad (4)$$

We can also construct a basis for the tensor components out of \mathbf{e}_1 and \mathbf{e}_2 by defining the following two matrices:

$$\begin{aligned} M_+ &= \mathbf{e}_1 \otimes \mathbf{e}_1 - \mathbf{e}_2 \otimes \mathbf{e}_2 \\ M_\times &= \mathbf{e}_1 \otimes \mathbf{e}_2 + \mathbf{e}_2 \otimes \mathbf{e}_1. \end{aligned} \quad (5)$$

Tensor components can then be written

$$T_{ij}^T = T_+^T (M_+)_{ij} + T_\times^T (M_\times)_{ij}. \quad (6)$$

B. Einstein Equations

We define perturbations of the conformally flat FRW metric as:

$$g_{\mu\nu} = a^2(\eta)(\eta_{\mu\nu} + h_{\mu\nu}), \quad (7)$$

where $\eta_{\mu\nu}$ is the Minkowski metric and $|h_{\mu\nu}| \ll 1$. We will work in the synchronous gauge in which $h_{00} = h_{0i} = 0$. This gauge is not completely specified. This will result in extra ‘‘constraint equations’’ from the Einstein equations, to ensure that all degrees of freedom are specified. Perturbations in the energy-momentum tensor are given by:

$$\begin{aligned} \delta T_0^0 &= -\delta\rho + \Theta_0^0 \\ \delta T_i^0 &= (\rho + p)v_i + \Theta_i^0 \\ \delta T_j^i &= \delta p \delta_j^i + p \Sigma_j^i + \Theta_j^i, \end{aligned} \quad (8)$$

where Θ_ν^μ is the energy momentum tensor of the causal stiff source and Σ_ν^μ contains the anisotropic stresses of relativistic matter. For the velocity terms, v_i and Θ_{0i} , we use slightly different variables to those defined in section II A:

$$\begin{aligned} \theta &= ikv^S, & \Theta_D &= ik\mathcal{P}^S \\ v_i^V &= i\tilde{v}_i^V, & \mathcal{P}_i^V &= i\tilde{\mathcal{P}}_i^V. \end{aligned} \quad (9)$$

These new variables enable us to write the evolution equation without explicit i 's, which is easier to implement numerically, as will be discussed in section IV.

The equations for $h_{\mu\nu}$ are then obtained by substituting equations (7) and (8) into the Einstein equations, using the homogeneous part for the background metric. The 00 and ij components of the equation

$$\delta(R_{\mu\nu} + \Lambda g_{\mu\nu}) = 8\pi G \delta(T_{\mu\nu} - \frac{1}{2} g_{\mu\nu} T_\lambda^\lambda) \quad (10)$$

then lead, to first order, after transforming to Fourier space and decomposing into SVT components, to the following equations of motion for h :

$$\begin{aligned} \ddot{h} + \frac{\dot{a}}{a} \dot{h} &= -8\pi G (a^2 (\delta\rho + 3\delta p) + \Theta_{00} + \Theta), \\ \ddot{h}^S + 2\frac{\dot{a}}{a} \dot{h}^S + \frac{k^2}{3} h^- &= 16\pi G (a^2 p \Sigma^S + \Theta^S), \\ \ddot{h}_i^V + 2\frac{\dot{a}}{a} \dot{h}_i^V &= 16\pi G (a^2 p \Sigma_i^V + \Theta_i^V), \\ \ddot{h}_\epsilon^T + 2\frac{\dot{a}}{a} \dot{h}_\epsilon^T + k^2 h_\epsilon^T &= 16\pi G (a^2 p \Sigma_\epsilon^T + \Theta_\epsilon^T), \end{aligned} \quad (11)$$

and the 00 and $0i$ components of the equation

$$\delta(R_{\mu\nu} - \frac{1}{2} R g_{\mu\nu} - \Lambda g_{\mu\nu}) = 8\pi G \delta T_{\mu\nu} \quad (12)$$

lead to the following constraint equations for h :

$$\begin{aligned} k^2 h^- + 3\frac{\dot{a}}{a} \dot{h} &= 24\pi G (a^2 \delta\rho + \Theta_{00}), \\ k^2 \dot{h}^- &= 24\pi G (\Theta_D - a^2 (\rho + p) \theta), \\ k \dot{h}_i^V &= 16\pi G (\tilde{\mathcal{P}}_i^V - a^2 (\rho + p) \tilde{v}_i^V), \end{aligned} \quad (13)$$

where $i = 1, 2$ and $\epsilon = +, \times$ and we have defined $h^- = h - h^S$.

Energy conservation $T^{\mu\nu}{}_{;\mu} = 0$ leads to the following equations of motion for matter and radiation perturbations:

$$\begin{aligned}\dot{\delta} &= -(1+w)(\theta + \frac{1}{2}\dot{h}) - 3\frac{\dot{a}}{a}(c_s^2 - w)\delta, \\ \dot{\theta} &= -\frac{\dot{a}}{a}(1 - 3c_s^2)\theta + \frac{c_s^2}{1+w}k^2\delta + \frac{2}{3}\frac{w}{1+w}k^2\Sigma^S, \\ \dot{\tilde{v}}_i^V &= -\frac{\dot{a}}{a}(1 - 3c_s^2)\tilde{v}_i^V - \frac{w}{1+w}k\Sigma_i^V,\end{aligned}\tag{14}$$

where $w = p/\rho$, $c_s^2 = \delta p/\delta\rho$ is the sound speed squared and $\delta = \delta\rho/\rho$. These equations are valid for uncoupled fluids. And covariant energy conservation with respect to the background $\Theta_{|\mu}^{\mu\nu}$ leads to

$$\begin{aligned}\dot{\Theta}_{00} &= -\frac{\dot{a}}{a}(\Theta_{00} + \Theta) + \Theta_D \\ \dot{\Theta}_D &= -2\frac{\dot{a}}{a}\Theta_D - \frac{k^2}{3}(\Theta + 2\Theta^S) \\ \dot{\tilde{\mathcal{P}}}_i^V &= -2\frac{\dot{a}}{a}\tilde{\mathcal{P}}_i^V + k\Theta_i^V.\end{aligned}\tag{15}$$

In what follows, we shall drop the tilde on the new variables to render the equations more legible.

C. Relativistic Matter

To treat photon perturbations, we derive the equations of motion for the Stokes parameters, which describe polarized light: the intensity I , the orientation of the polarization ellipse Q and U and the ratio of its principal axis V . It is convenient to work with the perturbations normalized to the average intensity $I_0 = \rho_\gamma/4\pi$:

$$\begin{aligned}I &= I_0(1 + \Delta_I), \\ P &= I_0\Delta_P,\end{aligned}\tag{16}$$

where P stands for Q, U or V . We start with the general transfer equations for polarized light:

$$\begin{aligned}\dot{\Delta}_I &= +ik\mu\Delta_I + 2\dot{h}_{ij}\hat{n}_i\hat{n}_j = \dot{\tau}(\Delta_I^S - \Delta_I + 4\hat{\mathbf{n}} \cdot \mathbf{v}_b), \\ \dot{\Delta}_P + ik\mu\Delta_P &= \dot{\tau}(\Delta_P^S - \Delta_P),\end{aligned}\tag{17}$$

where $\mu = \hat{\mathbf{n}} \cdot \hat{\mathbf{k}}$, $\dot{\tau} = a\sigma_T n_e$ is the differential Thompson cross-section, \mathbf{v}_b is the baryon velocity and the \mathcal{S} denotes scattered quantities as measured in the comoving frame and the vector Δ_P has Δ_Q, Δ_U and Δ_V as components. From the start, it is convenient to notice that V is always uncoupled to the other parameters as it cannot be generated through Thompson scattering. So we can set it to zero without loss of generality. We shall split the perturbations into scalar, vector and tensor parts: $\Delta_X = \Delta_X^S + \Delta_X^V + \Delta_X^T$, where $X = I, Q$ or U . The treatment for massless neutrinos is identical to that for the intensity of photons, except that all terms involving $\dot{\tau}$ are zero.

1. Scalar perturbations

For scalar modes, U is also uncoupled from I and Q , and hence can be set to zero. The contribution from the metric is

$$\hat{n}_i\hat{n}_j\dot{h}_{ij}^{scalar} = \frac{\dot{h}}{3} + (\mu^2 - \frac{1}{3})\dot{h}^S\tag{18}$$

and the ‘‘polarization term’’ is given by

$$\Delta_P^{SS}(\mu) = \frac{3}{16} \int_{-1}^1 M^S(\mu, \mu') \Delta_P^S(\mu') d\mu',\tag{19}$$

where the relevant block of the ‘‘scattering matrix’’ $M^S(\mu, \mu')$ is given by

$$\begin{pmatrix} 3 - \mu'^2 - \mu^2 + 3\mu^2\mu'^2 & 1 - \mu'^2 - 3\mu^2 + 3\mu^2\mu'^2 \\ 1 - 3\mu'^2 - \mu^2 + 3\mu^2\mu'^2 & 3 - 3\mu'^2 - 3\mu^2 + 3\mu^2\mu'^2 \end{pmatrix},\tag{20}$$

To integrate out the angle dependence, we expand the perturbations in Legendre polynomials:

$$\Delta_X^S = \sum_{\ell} (-i)^{\ell} (2\ell + 1) \Delta_{X\ell}^S P_{\ell}(\mu). \quad (21)$$

The equations then read

$$\begin{aligned} \dot{\Delta}_I^S + ik\mu + \frac{2}{3}(\dot{h} + (3\mu^2 - 1)\dot{h}^S) \\ = \dot{\tau}(\Delta_{I0}^S + 4\mu v_b^S - \Delta_I^S - \frac{1}{2}P_2(\mu)\Pi^S), \\ \dot{\Delta}_Q^S + ik\mu = \dot{\tau}(-\Delta_Q^S + (1 - \frac{1}{2}P_2(\mu))\Pi^S), \end{aligned} \quad (22)$$

where $\Pi^S = \Delta_{I2}^S + \Delta_{Q0}^S + \Delta_{Q2}^S$.

2. Vector Perturbations

Unlike scalar perturbations, U does not decouple from I and Q in the vector case, but this can be dealt with very easily. First we consider the contribution from the metric:

$$\hat{n}_i \hat{n}_j \dot{h}_{ij}^{vector} = 2\mu\sqrt{1-\mu^2}(\dot{h}_1^V \cos\varphi + \dot{h}_2^V \sin\varphi), \quad (23)$$

where $\cos\varphi = \hat{\mathbf{n}} \cdot \mathbf{e}_1$ and $\sin\varphi = \hat{\mathbf{n}} \cdot \mathbf{e}_2$. The polarization term is given by

$$\Delta_P^{VS}(\mu) = \frac{3}{16\pi} \int \sqrt{1-\mu^2} \sqrt{1-\mu'^2} M^V(\mu, \mu', \vartheta) \Delta_P^V(\mu') d\Omega', \quad (24)$$

where $\vartheta = \varphi' - \varphi$, and the scattering matrix $M^V(\mu, \mu', \vartheta)$ is given by:

$$\begin{pmatrix} 2\mu\mu' \cos\vartheta & 2\mu\mu' \cos\vartheta & \mu \sin\vartheta \\ 2\mu\mu' \cos\vartheta & 2\mu\mu' \cos\vartheta & \mu \sin\vartheta \\ -2\mu' \sin\vartheta & -2\mu' \sin\vartheta & \cos\vartheta \end{pmatrix}. \quad (25)$$

Unlike the scalar case, there is a dependence on the azimuthal angle. To eliminate it, we introduce new variables defined as follows:

$$\begin{aligned} \Delta_I^V &= -i\sqrt{1-\mu^2}(\Delta_I^{V1} \cos\varphi + \Delta_I^{V2} \sin\varphi) \\ \Delta_Q^V &= \mu\sqrt{1-\mu^2}(\Delta_Q^{V1} \cos\varphi + \Delta_Q^{V2} \sin\varphi) \\ \Delta_U^V &= \sqrt{1-\mu^2}(-\Delta_U^{V1} \sin\varphi + \Delta_U^{V2} \cos\varphi). \end{aligned} \quad (26)$$

With these variables, the equations for each components decouple and depend only on μ so that we can decompose the new variables into Legendre polynomials. The equations then read

$$\begin{aligned} \dot{\Delta}_I^{Vi} + ik\mu\Delta_I^{Vi} + 4i\mu\dot{h}_i^V &= -\dot{\tau}(\Delta_I^{Vi} - 4v_{bi}^V + i\mu\Pi^{Vi}), \\ \dot{\Delta}_Q^{Vi} + ik\mu\Delta_Q^{Vi} &= -\dot{\tau}(\Delta_Q^{Vi} - \Pi^{Vi}), \\ \dot{\Delta}_Q^{Vi} + \Delta_U^{Vi} &= 0, \end{aligned} \quad (27)$$

where $\Pi^{Vi} = \frac{3}{10}\Delta_{I1}^{Vi} + \frac{3}{10}\Delta_{I3}^{Vi} + \frac{13}{20}\Delta_{Q0}^{Vi} - \frac{3}{4}\Delta_{Q2}^{Vi} + \frac{6}{35}\Delta_{Q4}^{Vi}$.

3. Tensor Perturbations

Again, the Stokes parameter U cannot be set to zero, but, as with vector perturbations, we will show that can be treated with Q . The metric term is

$$\hat{n}_i \hat{n}_j \dot{h}_{ij}^{tensor} = (1 - \mu^2)(\dot{h}_+^T \cos 2\varphi + \dot{h}_\times^T \sin 2\varphi). \quad (28)$$

The polarization term is given by

$$\Delta^{TS}(\mu) = \frac{3}{32\pi} \int M^T(\mu, \mu', \vartheta) \Delta^T(\mu') d\Omega', \quad (29)$$

where the scattering matrix $M^T(\mu, \mu', \vartheta)$ is given by

$$\begin{pmatrix} S_-(\mu)S_-(\mu') \cos 2\vartheta & -S_-(\mu)S_+(\mu') \cos 2\vartheta & -\mu'S_-(\mu) \sin 2\vartheta \\ -S_+(\mu)S_-(\mu') \cos 2\vartheta & S_+(\mu)S_+(\mu') \cos 2\vartheta & \mu'S_+(\mu) \sin 2\vartheta \\ 2\mu S_-(\mu') \sin 2\vartheta & -2\mu S_+(\mu') \sin 2\vartheta & 2\mu\mu' \cos 2\vartheta \end{pmatrix}, \quad (30)$$

where $S_{\pm}(\mu) = 1 \pm \mu^2$.

As with the vector case, we can eliminate the φ dependence by making a change of variables. In the tensor case, these new variables are defined as follows:

$$\begin{aligned} \Delta_I^T &= (1 - \mu^2)(\Delta_I^{T+} \cos 2\varphi + \Delta_I^{T\times} \sin 2\varphi), \\ \Delta_Q^T &= (1 + \mu^2)(\Delta_Q^{T+} \cos 2\varphi + \Delta_Q^{T\times} \sin 2\varphi), \\ \Delta_U^T &= 2\mu(-\Delta_U^{T+} \sin 2\varphi + \Delta_U^{T\times} \cos 2\varphi). \end{aligned} \quad (31)$$

Exactly as for vectors, the equations for each polarization decouple and depend only on μ so that we can expand them in Legendre polynomials and carry out the integration. The resulting equations are:

$$\begin{aligned} \dot{\Delta}_I^{T\epsilon} + ik\mu\Delta_I^{T\epsilon} + 2\dot{h}_\epsilon^T &= -\dot{\tau}(\Delta_I^{T\epsilon} + \Pi^{T\epsilon}), \\ \dot{\Delta}_Q^{T\epsilon} + ik\mu\Delta_Q^{T\epsilon} &= -\dot{\tau}(\Delta_Q^{T\epsilon} - \Pi^{T\epsilon}), \\ \Delta_Q^{T\epsilon} + \Delta_U^{T\epsilon} &= 0, \end{aligned} \quad (32)$$

where $\Pi^{T\epsilon} = \frac{1}{10}\Delta_{I0}^{T\epsilon} + \frac{1}{7}\Delta_{I2}^{T\epsilon} + \frac{3}{70}\Delta_{I4}^{T\epsilon} - \frac{3}{5}\Delta_{Q0}^{T\epsilon} + \frac{6}{7}\Delta_{Q2}^{T\epsilon} - \frac{3}{70}\Delta_{Q4}^{T\epsilon}$ and $\epsilon = +$ or \times .

4. Physical significance of moments

If we use the decomposition (21) and the recursion relation

$$\mu P_\ell(\mu) = \frac{1}{2\ell+1}(\ell P_{\ell-1}(\mu) + (\ell+1)P_{\ell+1}(\mu)), \quad (33)$$

we obtain the following equations for the moments:

$$\begin{aligned} \dot{\Delta}_{I0}^S &= -k\Delta_{I1}^S - \frac{2}{3}\dot{h}, \\ \dot{\Delta}_{I1}^S &= -\frac{k}{3}(2\Delta_{I2}^S - \Delta_{I0}^S) - \dot{\tau}(\Delta_{I1}^S - \frac{4}{3k}\theta_b), \\ \dot{\Delta}_{I2}^S &= \frac{k}{5}(2\Delta_{I1}^S - 3\Delta_{I3}^S) - \dot{\tau}(\Delta_{I2}^S - \frac{1}{10}\Pi^S) - \frac{4}{15}\dot{h}^S, \\ \dot{\Delta}_{I\ell}^S &= \frac{-k}{2\ell+1}(\ell\Delta_{I\ell-1}^S - (\ell+1)\Delta_{I\ell+1}^S) - \dot{\tau}\Delta_{I\ell}^S, \quad \ell > 2, \\ \dot{\Delta}_{Q\ell}^S &= \frac{k}{2\ell+1}(\ell\Delta_{Q\ell-1}^S - (\ell+1)\Delta_{Q\ell+1}^S) + \dot{\tau}(-\Delta_{Q\ell}^S + \Pi^S(\delta_{\ell 0} + \frac{1}{10}\delta_{\ell 2})), \end{aligned} \quad (34)$$

$$\begin{aligned} \dot{\Delta}_{I0}^{Vi} &= -k\Delta_{I1}^{Vi} - \dot{\tau}(\Delta_{I0}^{Vi} + 4v_{bi}^V), \\ \dot{\Delta}_{I1}^{Vi} &= \frac{k}{3}(\Delta_{I0}^{Vi} - 2\Delta_{I2}^{Vi}) - \frac{4}{3}\dot{h}_i^V - \dot{\tau}(\Delta_{I1}^{Vi} + \Pi^{Vi}), \\ \dot{\Delta}_{I\ell}^{Vi} &= \frac{k}{2\ell+1}(\ell\Delta_{I\ell-1}^{Vi} - (\ell+1)\Delta_{I\ell+1}^{Vi}) - \dot{\tau}\Delta_{I\ell}^{Vi}, \quad \ell > 1, \\ \dot{\Delta}_{Q\ell}^{Vi} &= \frac{k}{2\ell+1}(\ell\Delta_{Q\ell-1}^{Vi} - (\ell+1)\Delta_{Q\ell+1}^{Vi}) - \dot{\tau}\Delta_{Q\ell}^{Vi} + \dot{\tau}\Pi^{Vi}\delta_{0\ell}, \end{aligned} \quad (35)$$

$$\begin{aligned} \dot{\Delta}_{I0}^{T\epsilon} &= -k\Delta_{I1}^{T\epsilon} - 2\dot{h}_\epsilon^T - \dot{\tau}(\Delta_{I0}^{T\epsilon} + \Pi^{T\epsilon}), \\ \dot{\Delta}_{I\ell}^{T\epsilon} &= \frac{k}{2\ell+1}(\ell\Delta_{I\ell-1}^{T\epsilon} - (\ell+1)\Delta_{I\ell+1}^{T\epsilon}) - \dot{\tau}\Delta_{I\ell}^{T\epsilon}, \quad \ell > 0, \\ \dot{\Delta}_{Q\ell}^{T\epsilon} &= \frac{k}{2\ell+1}(\ell\Delta_{Q\ell-1}^{T\epsilon} - (\ell+1)\Delta_{Q\ell+1}^{T\epsilon}) - \dot{\tau}\Delta_{Q\ell}^{T\epsilon} - \dot{\tau}\Pi^{T\epsilon}\delta_{\ell 0}. \end{aligned} \quad (36)$$

These moments are related to the energy momentum tensor of photons and (massless) neutrinos. First, let us consider the energy density. We have that

$$\delta T_{00} = -\delta\rho = -\frac{\rho}{4\pi} \int \Delta_I d\Omega, \quad (37)$$

so that

$$\delta = \Delta_{I0}^S. \quad (38)$$

Secondly, the velocity perturbations

$$\delta T_{0i} = (\rho + p)v_i = \frac{3p}{4\pi} \int \Delta_I \hat{n}_i d\Omega, \quad (39)$$

which yields

$$\begin{aligned} \theta &= \frac{3}{4}k\Delta_{I1}^S, \\ v_i^V &= \frac{1}{4}(\Delta_{I0}^{Vi} + \Delta_{I2}^{Vi}). \end{aligned} \quad (40)$$

Finally we have the anisotropic stresses

$$\delta T_{ij} - \frac{1}{3}T_k^k \delta_{ij} = p\Sigma_{ij} = \frac{3p}{4\pi} \int \Delta_I (\hat{n}_i \hat{n}_j - \frac{1}{3}\delta_{ij}) d\Omega, \quad (41)$$

which yields

$$\begin{aligned} \Sigma^S &= -3\Delta_{I2}^S, \\ \Sigma_i^V &= \frac{3}{5}(\Delta_{I1}^{Vi} + \Delta_{I3}^{Vi}), \\ \Sigma_\epsilon^T &= \frac{2}{5}\Delta_{I0}^{T\epsilon} + \frac{4}{7}\Delta_{I2}^{T\epsilon} + \frac{6}{35}\Delta_{I4}^{T\epsilon}. \end{aligned} \quad (42)$$

We now have an open hierarchy of equations for all the components of the energy-momentum tensor. Numerically, it has been found that truncating the expansion by simply setting the ℓ^{th} moment to 0 propagates a sizeable error back to the first moment. It has also been found [23] that the following expression gives excellent results:

$$\dot{\Delta}_{\ell_{max}} = k\Delta_{\ell_{max}-1} - \left(\frac{\ell_{max}-1}{\eta} + \dot{\tau} \right) \Delta_{\ell_{max}}, \quad (43)$$

where ℓ_{max} is the moment at which the series is truncated. The above expression is good for all photon and neutrino equation hierarchies.

D. Non-Relativistic Matter

For non-relativistic matter, it is not necessary to consider a full phase space expansion, as all but the first few moments are totally negligible. Our starting point will be the equations derived from the conservation of the energy-momentum tensor (14).

CDM does not couple with other types of matter (except gravitationally), so we can immediately use the conservation equations. Here $w = c_s^2 = 0$. Also, in the (comoving) synchronous gauge, CDM has $\mathbf{v}_c = \Sigma_{ij} = 0$, so (14) simplifies to

$$\dot{\delta}_c = -\frac{\dot{h}}{2}. \quad (44)$$

For baryons, these conservation equations (14) become

$$\begin{aligned} \dot{\delta}_b &= -(\theta_b + \frac{\dot{h}}{2}) \\ \dot{\theta}_b &= -\frac{\dot{a}}{a}\theta_b + c_s^2 k^2 \delta_b \\ \dot{v}_{bi}^V &= -\frac{\dot{a}}{a}v_{bi}^V, \end{aligned} \quad (45)$$

where we have used the fact that $w, c_s^2 \ll 1$. However, baryons interact with photons through Thompson scattering. So we must correct the last two equations for momentum exchange between the two fluids. The equations for photons obtained in section II C 4 read

$$\begin{aligned} \dot{\theta}_\gamma &= k^2(\frac{1}{4}\delta_\gamma - \frac{1}{6}\Sigma^S) + \dot{\tau}(\theta_b - \theta_\gamma) \\ \dot{v}_{\gamma i}^V &= \frac{k}{4}\Sigma_{\gamma i}^V + \dot{\tau}(v_{bi}^V - v_{\gamma i}^V). \end{aligned} \quad (46)$$

By comparing with the conservation equations with $w = c_s^2 = \frac{1}{3}$, we see that there is an extra drag term $\dot{\tau}(v_b - v_\gamma)$. Hence, for momentum to be conserved, we have to add the term $\frac{4\rho_\gamma}{3\rho_b}\dot{\tau}(v_\gamma - v_b)$ to the previous two equations, which then become

$$\begin{aligned} \dot{\theta}_b &= -\frac{\dot{a}}{a}\theta_b + c_s^2 k^2 \delta_b + R\dot{\tau}(\theta_\gamma - \theta_b) \\ \dot{v}_{bi}^V &= -\frac{\dot{a}}{a}v_{bi}^V + R\dot{\tau}(v_{\gamma i}^V - v_{bi}^V). \end{aligned} \quad (47)$$

where we have defined $R = \frac{4\rho_\gamma}{3\rho_b}$.

E. The Sachs-Wolfe Formula

The temperature anisotropy formula is derived by considering perturbations in the photon energy E_γ along the unperturbed path $X^\mu = \hat{n}^\mu \eta$. Here $\hat{\mathbf{n}}$ is the line of sight direction (i.e. pointing in the direction opposite to the photon's travel). For a proof, see e.g. [12, 25]. In the synchronous gauge, the temperature fluctuations are given by:

$$\frac{\delta T}{T} = \frac{\delta_\gamma}{4} - \mathbf{v}_\gamma \cdot \hat{\mathbf{n}} - \frac{1}{2} \int \dot{h}_{ij} \hat{n}_i \hat{n}_j d\eta. \quad (48)$$

The above formula was derived under the assumption of instantaneous recombination. To treat the finiteness of the surface of last-scattering, we integrate the expression for the temperature fluctuations over the probability of free-streaming for a photon, $e^{-\tau} d\tau$:

$$\frac{\overline{\delta T}}{T} = \int_0^{\eta_0} \frac{\delta T}{T} \dot{\tau} e^{-\tau} d\eta = \int_0^{\eta_0} \left(\dot{\tau} e^{-\tau} \left(\frac{\delta_\gamma}{4} - \mathbf{v}_\gamma \cdot \hat{\mathbf{n}} \right) - \frac{1}{2} e^{-\tau} \dot{h}_{ij} \hat{n}_i \hat{n}_j \right) d\eta, \quad (49)$$

where the ISW term was obtained by integrating by parts and setting the surface term to zero because the visibility function is very sharply defined around the time of recombination and hence is utterly negligible at $\eta = 0$ or today.

The calculation of the thermal history of the universe for an arbitrary set of cosmological parameters was achieved with an integrated package which will be described in more detail elsewhere [26]. The Friedmann equations were solved simultaneously with the ionization rate equations for hydrogen and helium. The results were compared for accuracy against RECFAST [27] for which the code provided an independent check [26]. These computations start very deep in the radiation era and end today in order to create high accuracy tables from which the relevant quantities for the Boltzmann evolution, such as the opacity and visibility function, are later interpolated using a cubic spline.

III. COSMIC DEFECT SOURCE TERMS

The perturbation source terms in the Boltzmann evolution are given by the Fourier transform of the cosmic defect energy-momentum tensor, decomposed into scalar, vector and tensor components. The code can accept the energy-momentum tensor of any set of 'active' sources with appropriate initial conditions, whether these are cosmic strings, global defects or other more exotic phenomena. We have experimented with inputting from global defect simulations, but the focus of our attention here is on local cosmic string simulations which inherently can achieve far higher resolution and greater dynamic range.

The cosmic string simulations were performed using the AS code [15], for which the methods employed and key results have been described in detail elsewhere. The strings are approximated by a two-dimensional worldsheet defined by $x_s^\mu(\sigma, t) = (t, \mathbf{x}_s(\sigma, t))$, where the position \mathbf{x}_s is a function of the two coordinates σ (spacelike) and conformal time t in an unperturbed FRW background. We can impose the condition that the velocity $\dot{\mathbf{x}}$ is transverse to the tangent vector $\mathbf{x}'_s \equiv d\mathbf{x}_s/d\sigma$ along the string, that is, $\dot{\mathbf{x}}_s \cdot \mathbf{x}'_s = 0$. The strings are evolved by splitting the equations of motion for the strings into their characteristic left- and right-moving modes, which are damped slightly by the expansion of the universe. The key points to note about the string network simulations are that above a minimum resolution, energy conservation is accurately satisfied during the numerical evolution to within a fraction of one percent, and over a dynamic range approaching an order of magnitude in conformal time (that is, several decades in redshift).

The energy-momentum tensor of the strings is given by

$$\Theta^{\mu\nu} \sqrt{-g} = \mu_s \int d\sigma (\epsilon \dot{x}_s^\mu \dot{x}_s^\nu - \epsilon^{-1} x_s'^\mu x_s'^\nu) \delta^{(3)}(\mathbf{x}^\sigma - \mathbf{x}_s^\sigma(\sigma)), \quad (50)$$

where μ_s is the linear energy density of the string, $\epsilon = (\mathbf{x}'^2/(1 - \dot{\mathbf{x}}^2))^{1/2}$, and g is the determinant of the background FRW metric ($\sqrt{-g} = a^4$). All the components of $\Theta_{\mu\nu}(\mathbf{x}, \eta)$ were calculated at each point on the string network and then interpolated onto a high resolution grid. Since there is an implicit differentiation of the spatial distribution of (50) in the scalar-vector-tensor decomposition described in section II A, the interpolation must be sufficiently smooth for the decomposition to remain well behaved. Simple cloud-in-cell interpolation, for example, produced poorly controlled results, so we chose a two step approach with a higher order scheme. The first step was to use the triangular shaped cloud (TSC) interpolation involving the 27 nearest neighbour points of the string segment. The weight function is given by

$$W_3(x) = \begin{cases} \frac{3}{4} - x^2, & |x| < \frac{1}{2}, \\ \frac{1}{2} \left(\frac{3}{2} - x^2 \right)^2, & \frac{1}{2} < |x| \leq \frac{3}{2}, \end{cases}$$

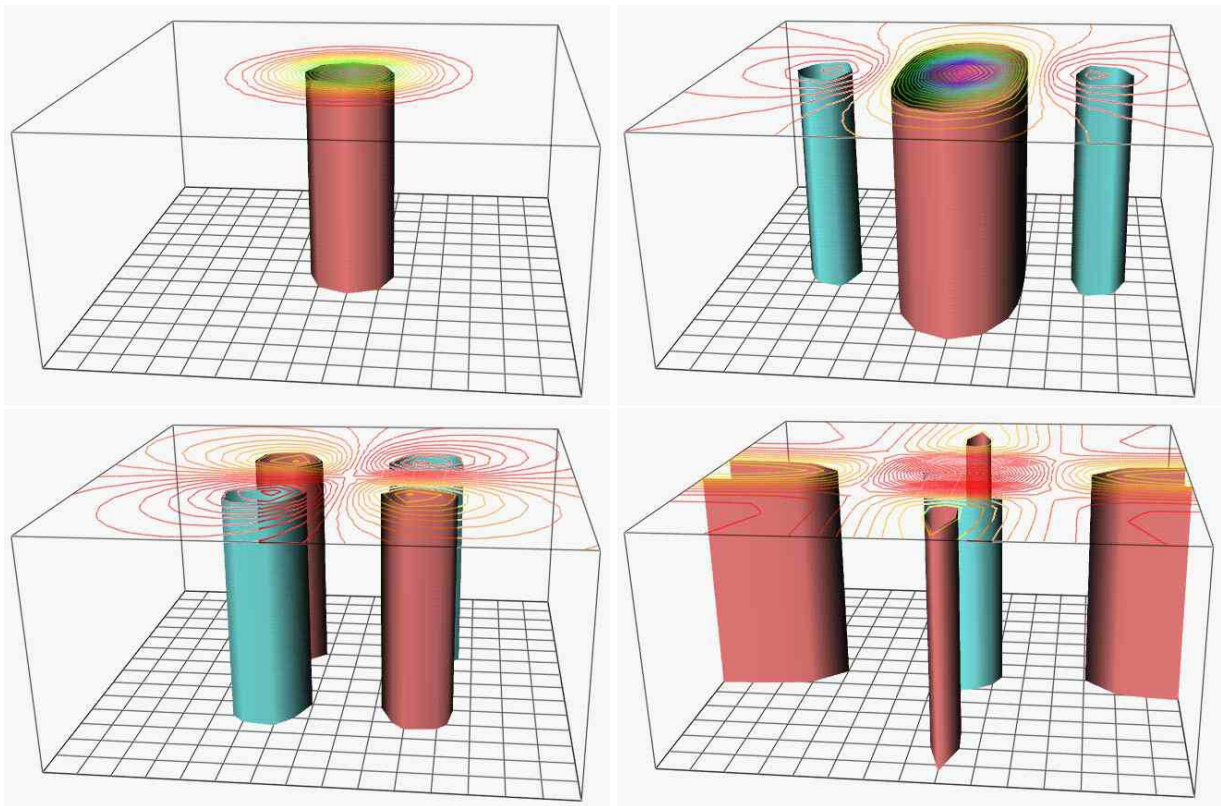


FIG. 1: Positive and negative isosurfaces of scalar, vector and tensor components in real space created from the decomposition of the energy-momentum tensor of a straight string. Clockwise from top-left Θ_{00} (positive), Θ_S (positive centre and negative sidelobes), Θ_T^+ (negative centre and positive sidelobes) and Θ_V^1 (alternating negative and positive). Also shown are contours in a plane transverse to the string.

where $|x|$ is the distance between grid point and string in the x -direction. This weight function is multiplied by the appropriate weights in y - and z -directions. The second step is to smooth the result further by employing a gaussian window function in Fourier space, that is, proportional to $\exp(-k^2/k_R^2)$ with k_R^{-1} corresponding to about three grid points; the discrete Fourier transform employed the NAG routine C06PKF. Energy-momentum conservation was closely monitored and maintained to within a fraction of one percent by this process.

The smoothing from the interpolation and filtering leads to an apparent loss of resolution, but this need not be important. A well-behaved decomposition can be obtained at very high resolution on a larger grid and then used at lower resolution for the Green's function integration. We note also that, in Fourier space, the decomposed scalar, vector and tensor parts of (50) calculated as in section II A can be stored on only half the complex grid, because the Fourier transform of a real quantity satisfies $f(\mathbf{k}) = f^*(-\mathbf{k})$, it is necessary to treat only just over half of the grid, that is, $i_x, i_y = 0, 1, \dots, N-1$ and $i_z = 0, 1, \dots, N/2$ (it is in fact possible to use exactly half, but the relationship between components is more complicated [28]).

Figure 1 illustrates the decomposed scalar, vector and tensor parts of (50) for a straight cosmic string calculated as in section II A. The scalar Θ_{00} is localised in real space, but the scalar and vector projection operators acting on the tensor components Θ_{ij} yields the apparently non-local results shown. This demonstrates that the decomposed components must be calculated and evolved with great care; the final temperature pattern must reflect the locality (or causality) of the sources which generated them.

IV. NUMERICAL IMPLEMENTATION

The various evolution equations derived in section II can be written as three systems (one for scalar, vector and tensor) of the following form:

$$\frac{dy}{d\eta} = \mathcal{A}(k, \eta)\mathbf{y} + \mathbf{q}(k, \eta), \quad (51)$$

where \mathbf{y} and \mathbf{q} are vectors of dimension n_{var} , the number of equations to solve and \mathcal{A} is a real square matrix of the same order. The components of \mathbf{y} are the metric perturbation, CDM and baryon density contrasts and peculiar velocities and photon and neutrino moments and those of \mathbf{q} are the defect source terms. Given that there is a continuous contribution at all times from these sources throughout space, we cannot simply solve this problem by projecting our initial conditions forward to the present time with transfer functions (as in inflation). However, rather than directly solving the differential equations at every grid point, it is much more efficient to employ a Green's function approach.

In order to take advantage of the fact that the evolution equations depend only on the magnitude of the wavevector and not its orientation, we proceed to solve (51) by constructing the fundamental matrix Y of the system (e.g. see [29]) which satisfies

$$\begin{aligned} \frac{d}{d\eta} Y &= \mathcal{A}Y, \\ Y(0) &= \mathbf{1}, \end{aligned} \quad (52)$$

where $\mathbf{1}$ is the identity matrix. Now, given some initial conditions

$$\mathbf{y}(0) = \mathbf{c}, \quad (53)$$

the solution to (51) is

$$\mathbf{y}(\eta) = Y(\eta) \left(\mathbf{c} + \int_0^\eta Y^{-1}(\eta') \mathbf{q}(\eta') d\eta' \right). \quad (54)$$

The above equation reveals a similarity between the matrix Y^{-1} and a Green's function. However, the latter nomenclature is not strictly appropriate in this case, as one of the basic properties of a Green's functions is undefined in a first order problem.

A. Constructing the Matrices

Since the system (51) is first order, we need to reexpress the metric equations in first order form (all the matter equations are already first order). For the scalar metric equations, we use the two equations of motion, with the first constraint equation to replace the $k^2 h^-$ term, to obtain the following first order equations for \dot{h} and \dot{h}^S :

$$\begin{aligned} \frac{d\dot{h}}{d\eta} &= -\frac{\dot{a}}{a} \dot{h} - 8\pi G a^2 (\delta\rho + 3\delta p) - 8\pi G (\Theta_{00} + \Theta), \\ \frac{d\dot{h}^S}{d\eta} &= \frac{\dot{a}}{a} (\dot{h} - 2\dot{h}^S) + 8\pi G a^2 (2p\Sigma^S - \delta\rho) + 8\pi G (2\Theta^S - \Theta_{00}). \end{aligned} \quad (55)$$

The vector metric equation of motion is already in a form that is first order for \dot{h}^V :

$$\frac{d\dot{h}^V}{d\eta} = -2\frac{\dot{a}}{a} \dot{h}^V + 16\pi G a^2 p\Sigma^V + 16\pi G \Theta^V. \quad (56)$$

For the tensor modes, we use the standard order reduction, by considering h^T and \dot{h}^T as separate variables:

$$\begin{aligned} \frac{dh^T}{d\eta} &= \dot{h}^T, \\ \frac{d\dot{h}^T}{d\eta} &= -2\frac{\dot{a}}{a} \dot{h}^T - k^2 h^T + 16\pi G a^2 p\Sigma^T + 16\pi G \Theta^T. \end{aligned} \quad (57)$$

To construct Y , we numerically solve (52), which involves solving 3 times (scalar - vector - tensor) n_{var} systems of n_{var} coupled equations for a chosen number M of the wavenumbers k (typically $M \sim N$ for an N^3 grid). This contrasts with solving 10 systems (real and imaginary parts of 1 scalar, 2 vectors and 2 tensors) of n_{var} equations for $N^3/2$ wavevectors \mathbf{k} if we were to solve (51) directly at every grid point. Hence this Green's function approach represents a reduction of computing time by a factor of $5N^2/3n_{var}$. Since $n_{var} \simeq 40$, this factor is more than 1,000 for a 256^3 box and 10,000 for a 1024^3 box. Of course, there are extra computations involved: the inversion of the matrices (for which we use the NAG F07ADF and F07ADJ Fortran routines) and the actual integration of (54), but this is insignificant compared with the time taken to solve the extra equations. In fact, this method is so efficient it is constrained by the amount of memory (or disk space) required.

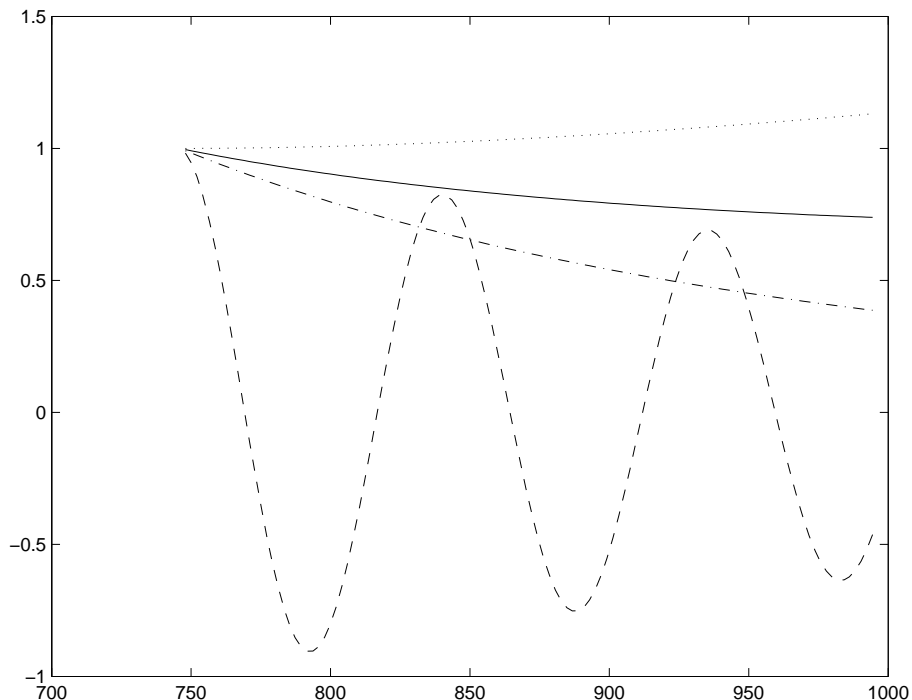


FIG. 2: Time evolution of elements of the fundamental matrices for $\eta = 3\eta_{dec}$ to $4\eta_{dec}$. These particular diagonal elements are those associated with ISW effects, i.e. the time derivative of the metric terms: scalar trace \dot{h} (solid), anisotropic scalar \dot{h}^S (dot-dashed), which coincides with the vector \dot{h}^V and tensor \dot{h}^T (dashed). Also illustrated is the CDM density contrast δ_c (dotted). The conformal time along the horizontal axis is given in Mpc

To numerically solve the perturbation equations, we use `dverk.f`, a sixth order Runge-Kutta Fortran routine. Figure 2 shows the time evolution for some diagonal elements of the fundamental matrices. Our Boltzmann code was extensively tested for inflationary scenarios and found to be in excellent agreement with publicly available codes [26]. The matrix elements are computed for $k = 0$ to $k = 1.8N\Delta k/2$ with a spacing of $0.9\Delta k$, where Δk is the simulation grid spacing. The value of 1.8 was chosen to be slightly higher than the maximum possible value $\sqrt{3}$. This is to ensure that there is no need to extrapolate the matrix elements. This k -spacing is sufficiently dense for the elements of the matrices and their inverses to be linearly interpolated for the appropriate value of k at every simulation grid point (see FIG. 3).

Since only a few components of the vector \mathbf{q} are non-zero (two for scalars, one for vectors and one for tensors), only the corresponding rows of Y^{-1} need to be stored. Also, since only 10 quantities are needed to compute the SW integral (δ_γ , θ_γ , v_γ^V , h , h^S , h^V and h^T), only the corresponding columns of Y need to be stored in principle. In practise however, all components y need to be kept to allow the computations to be made in several stages. There are two reasons why we want to do this. The main reason is that, even though all the components of the fundamental matrices are well behaved at all times, the evolution results in different components having very large ratios. This results in Y become non-invertible *to machine precision*. This happens more often at early times and for scalar modes. The solution (54) is then computed by

$$\begin{aligned} \mathbf{y}(\eta) &= Y^{(i)}(\eta) \left(\mathbf{y}(\eta_i) + \int_{\eta_i}^{\eta_{i+1}} Y^{(i)-1}(\eta') \mathbf{q}(\eta') d\eta' \right) \\ \eta_i &< \eta < \eta_{i+1}, \quad i = 0, 1, \dots, n_{stage} \\ \mathbf{y}(\eta_{i=0}) &= \mathbf{c}, \end{aligned} \quad (58)$$

where the corresponding matrices $Y^{(i)}$ and $Y^{(i)-1}$ are computed from η_i to η_{i+1} . The second reason for wanting to allow the possibility of running the computations in several stages is more practical: this enables us to checkpoint the code in order minimize the effects of a system crash.

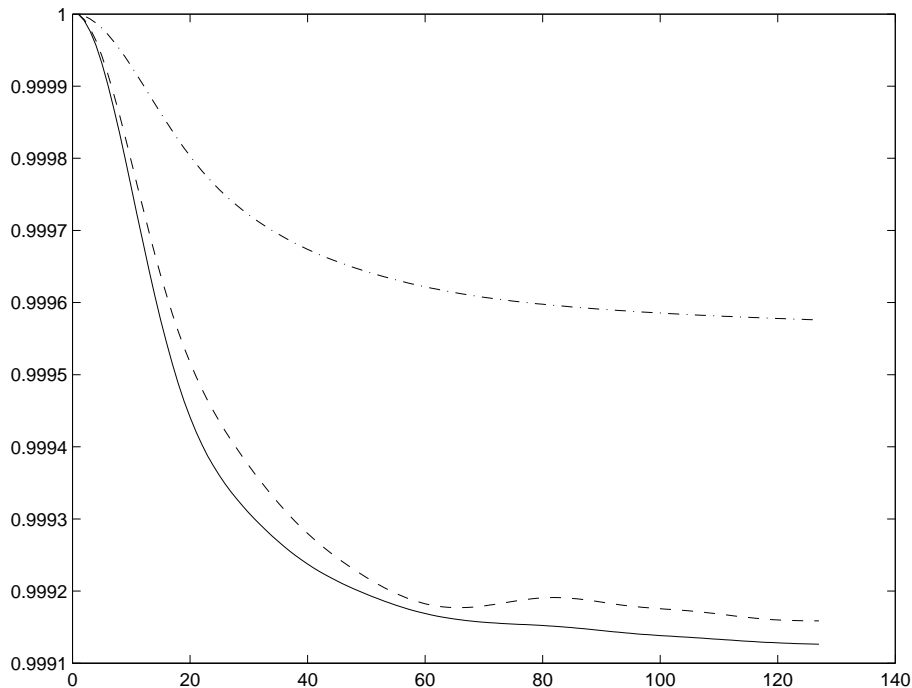


FIG. 3: Diagonal scalar matrix elements Y_{11} , Y_{11}^{-1} and Y_{33} from the late matter era corresponding respectively to \dot{h} (continuous and dashed lines) and δ_c (dot-dashed). The normalisation is arbitrary and the k scale is $1.8 \times 10^{-4} Mpc^{-1}$.

B. Initial Conditions

As our simulations start at a time much later than that of the phase transition that created the defects, we must specify initial conditions that are consistent with a fully formed network. In any case, the local string simulations used are based on an effective action and hence cannot be used to simulate the phase transition itself.

One of the nice things about the solution (54) is that it is expressed as a sum of a term depending on the initial conditions and a second one depending on the defect sources. This provides us with an easy way to assess the relative importance of the initial conditions and hence to see if our results are sensitive or not to them.

One possible choice is to set all gradient terms and time derivatives to zero in the constraint equations. This leads to the following initial conditions:

$$\begin{aligned} \delta_c = \delta_b = \frac{3}{4}\delta_\gamma = \frac{3}{4}\delta_\nu &= -\frac{\Theta_{00}}{a^2(\rho+p)}, \\ \theta_b = \theta_\gamma = \theta_\nu &= \frac{\Theta_p}{a^2(\rho+p)}, \\ v_b^V = v_\gamma^V = v_\nu^V &= \frac{\mathcal{P}^V}{a^2(\rho+p)}, \end{aligned} \quad (59)$$

the last line being valid for all three components. This choice is consistent with setting the pseudo-energy τ_{00} and pseudo-momenta τ_{0i} to zero, a set of initial conditions consistent with matching an instantaneous defect-forming phase transition to a homogeneous initial state (see, for example, [30, 31]).

C. Integration over the String Energy-Momentum Tensor

The matrix elements are integrated over the energy-momentum tensor using the trapezoidal rule. The equations being real and scalar, the same matrices are used for both the real and imaginary parts as well as the two vector and two tensor components, so that the integration is repeated twice for scalars, and four times for both vectors and tensors.

The grids of the quantities needed to compute the SW integral, δ_γ , \mathbf{v}_γ and h_{ij} are then completed at each timestep by complex conjugation and Fourier transformed back to real space. They are then projected onto the end of the

vectors $\hat{n}_i(\eta - \eta_0)$, where the \hat{n}_i are the pixel directions, using the inverse cloud-in-cell scheme:

$$\begin{aligned} f(x, y, z) = & w_x(w_y(w_z f(x_1, y_1, z_1) + (1 - w_z)f(x_1, y_1, z_2)) \\ & + (1 - w_y)(w_z f(x_1, y_2, z_1) + (1 - w_z)f(x_1, y_2, z_2))) \\ & + (1 - w_x)(w_y(w_z f(x_2, y_1, z_1) + (1 - w_z)f(x_2, y_1, z_2)) \\ & + (1 - w_y)(w_z f(x_2, y_2, z_1) + (1 - w_z)f(x_2, y_2, z_2))), \end{aligned} \quad (60)$$

where the x_1, x_2, \dots define the grid element and the weights are given by $w_x = 1 - x_1$ and similarly for the other two. The temperature fluctuations are then computed using (49). This integration is also performed using the trapezoidal rule as the integrand varies very smoothly along each line of sight.

V. TEST OF THE NUMERICS

In order to test the validity of our methods, we compare the result of simulations with analytic results. One of the difficult aspects of such comparisons is that analytic results are mostly obtained for defect configurations (i) in Minkowski space and (ii) in the no matter approximation. In an expanding Universe, with a complete treatment of matter perturbations, these approximations would be relatively good only in the late matter era and on scales much smaller than the horizon.

A. Kaiser-Stebbins Effect

To illustrate this, we consider an infinite straight string moving in a direction perpendicular to the line-of-sight. According to [8], this will produce a discontinuity in the temperature fluctuations. This calculation is done in the limit that a plane wave of CMB radiation is propagating in the direction of the observer. Objects behind the string receive a boost towards the plane in which the string is moving because of the gravitational effect of its deficit angle $\Delta = 8\pi G\mu$. This means that the CMB photons that were behind the string when they cross its plane will be blueshifted, so that they will be hotter than those that were in front of the string. The magnitude of the discontinuity is [9]:

$$\frac{\Delta T}{T} = 8\pi G\mu v\gamma, \quad (61)$$

where v is the string velocity and γ is the Lorentz factor.

This provides an excellent test of our map-making pipeline, particularly the vector modes, which cannot be compared with inflationary results such as is done for the scalars and tensors in chapter [26]. However, in a realistic expanding Universe, such as those studied in this dissertation, this effect is more complicated due to the presence of matter, the growth (or decay) of SVT components, the curvature of the microwave sky and the deceleration of the string. In addition, this idealised solution must be studied in a periodic box with causal effects due to the limited dynamic range.

In the realisation shown in figure 4, we minimised these effects by considering photon propagation in the late Universe with no cosmological constant, starting at $\eta = 0.34\eta_0$ and ending at $\eta = 0.41\eta_0$, on a square patch of sky of $3.2^\circ \times 3.2^\circ$ through a box of comoving size $L = 0.069\eta_0$. The string was initially moving at a velocity $v = 0.9$, which had redshifted to $v = 0.825$ as the photons crossed the plane of the string. These test simulations included no compensation, i.e. everything was set to zero initially. The temperature jump measured from the average of the plateaus behind and in front of the string is approximately

$$\frac{\Delta T}{T} \simeq 53G\mu/c^2, \quad (62)$$

whereas the theoretical flat-space, vacuum (no matter) prediction for the given velocities should lie in the range:

$$\frac{\Delta T}{T} \simeq (37 - 52)G\mu/c^2. \quad (63)$$

This is in good agreement with the expanding Universe simulation, despite the additional physical effects involved. It appears that the effect of matter on the scalar and vector modes slightly increases the anisotropies over the dominant flat-space ISW effect.

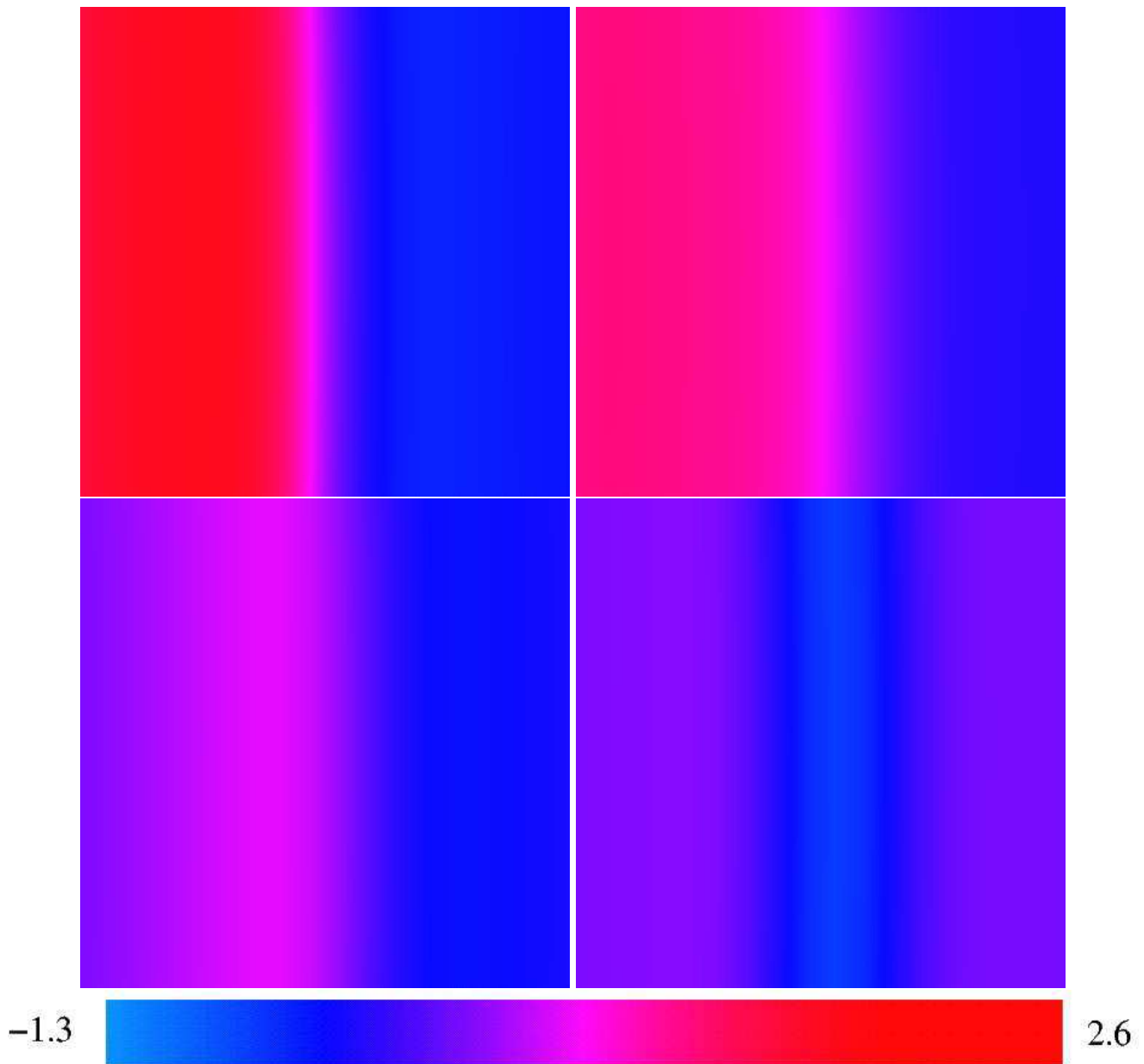


FIG. 4: Temperature discontinuity induced by a straight moving string with an initial velocity $v = 0.9$: total (top-left), scalar (top-right), vector (bottom-left) and tensor (bottom-right). The colour scale is given in units of $\Delta = 8\pi G\mu/c^2$

B. Loop Anisotropies

In this subsection, we show the results of small angular scale simulations of string loops of radius $R = 0.5\eta$. The size of the horizon at the *beginning* of the simulation is $0.5L$ where L is the size of the box. The simulations end at $\eta \approx 10\eta_{dec}$. Hence, we are dealing with large loops smaller than the horizon, but initially perturbed by Hubble damping.

The general loop solution in flat-space can be expanded in Fourier modes, with the gauge conditions yielding constraints on the relationship between the different modes. These can be solved if only the first few harmonics are considered. The Kibble-Turok solution [32] for a loop of length L involves the first and third harmonics:

$$\mathbf{x}(\zeta, t) = \frac{L}{4\pi} \left\{ \hat{\mathbf{e}}_1 \left[(1 - \kappa) \sin \sigma_- + \frac{1}{3} \kappa \sin 3\sigma_- + \sin \sigma_+ \right] \right. \\ \left. - \hat{\mathbf{e}}_2 \left[(1 - \kappa) \cos \sigma_- + \frac{1}{3} \kappa \cos 3\sigma_- + \cos \varphi \cos \sigma_+ \right] \right. \\ \left. - \hat{\mathbf{e}}_3 \left[2\kappa^{1/2} (1 - \kappa)^{1/2} \cos \sigma_- + \sin \varphi \cos \sigma_+ \right] \right\}, \quad (64)$$

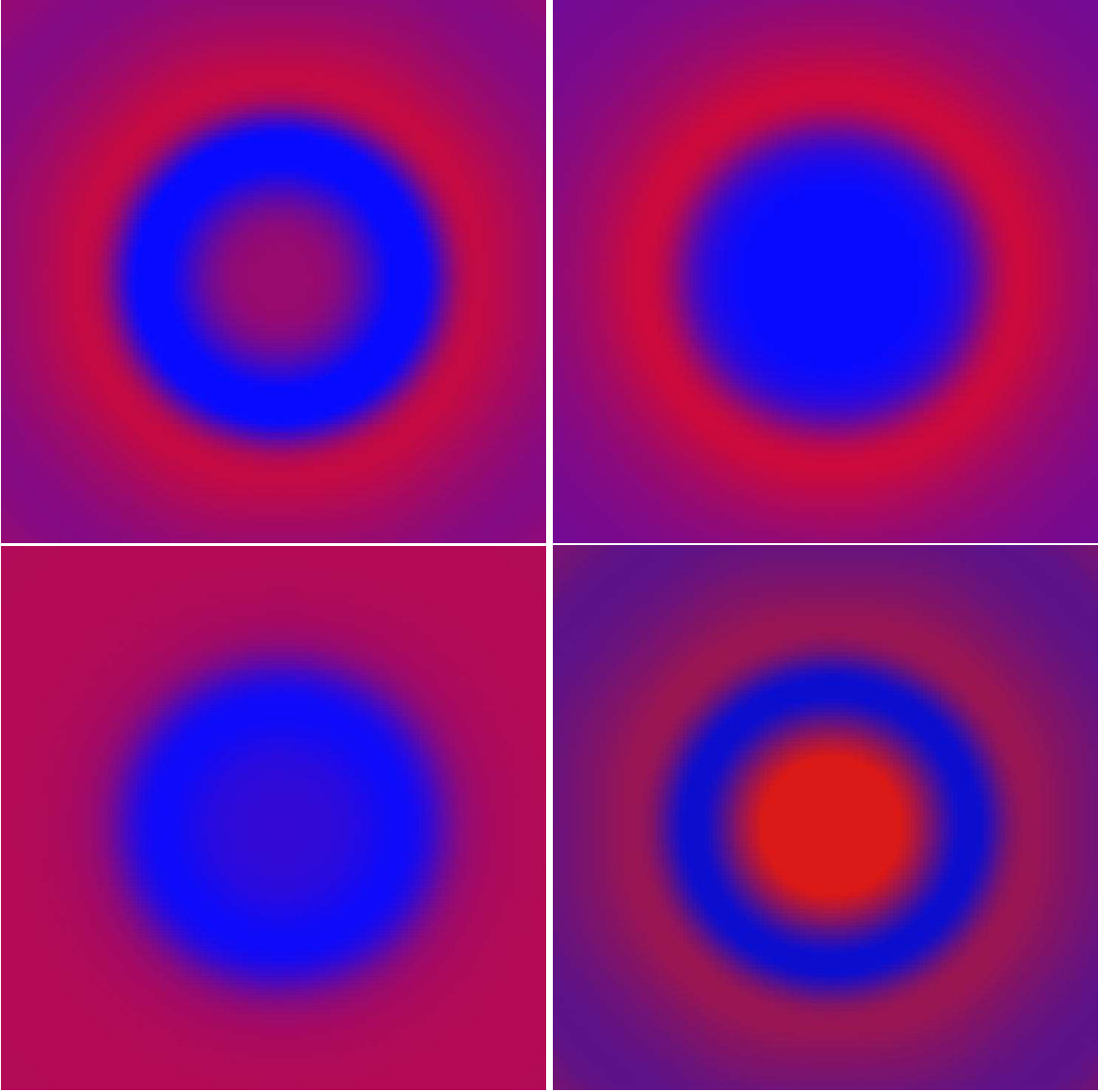


FIG. 5: CMB fluctuations seeded by a single loop: total (top-left), scalar (top-right), vector (bottom-left) and tensor (bottom-right).

where $\sigma_{\pm} = (2\pi/L)\zeta_{\pm}$ are the left/right moving modes and the $\hat{\mathbf{e}}_i$ are the cartesian unit vectors.

Figure 5 shows the CMB fluctuations caused by a perfectly circular loop ($\varphi = \kappa = 0$). The loop has an initial radius just below the angular scale of the patch shown in figure 5. The loop begins stationary and then accelerates up to a relativistic velocity as it collapses. At this point it is crossed by the plane of CMB photons where a clear Kaiser-Stebbins discontinuity is evident; note that the amplitude of the temperature increases from large to small radius as the velocity increases. There is a cancellation of the non-local scalar, vector and tensor modes in the interior. By the time of photon crossing, causal effects related to the velocity acceleration have not had time to propagate to the centre. During one period, the average velocity of a loop is $\langle v \rangle = 1/\sqrt{2}$.

Next we consider a loop with $\varphi = \pi/3$ and $\kappa = 1/2$, which does not possess the simple symmetries of the circular case. Its initial state is one of maximum radius and minimum velocity from which it then shrinks, accelerates and begins to rotate and form cusps. Figure 6 illustrates the total anisotropy pattern viewed from three different directions into the box. In the top right corner, there are two things to note: when the photons first cross the loop, there is little effect as it is moving slowly; whereas there is a strong discontinuity later when the photons pass the front of the relativistically collapsing loop. The bottom left corner shows a side view of the loop, while the bottom right shows a much more complex anisotropy pattern as cusps form viewed from above.

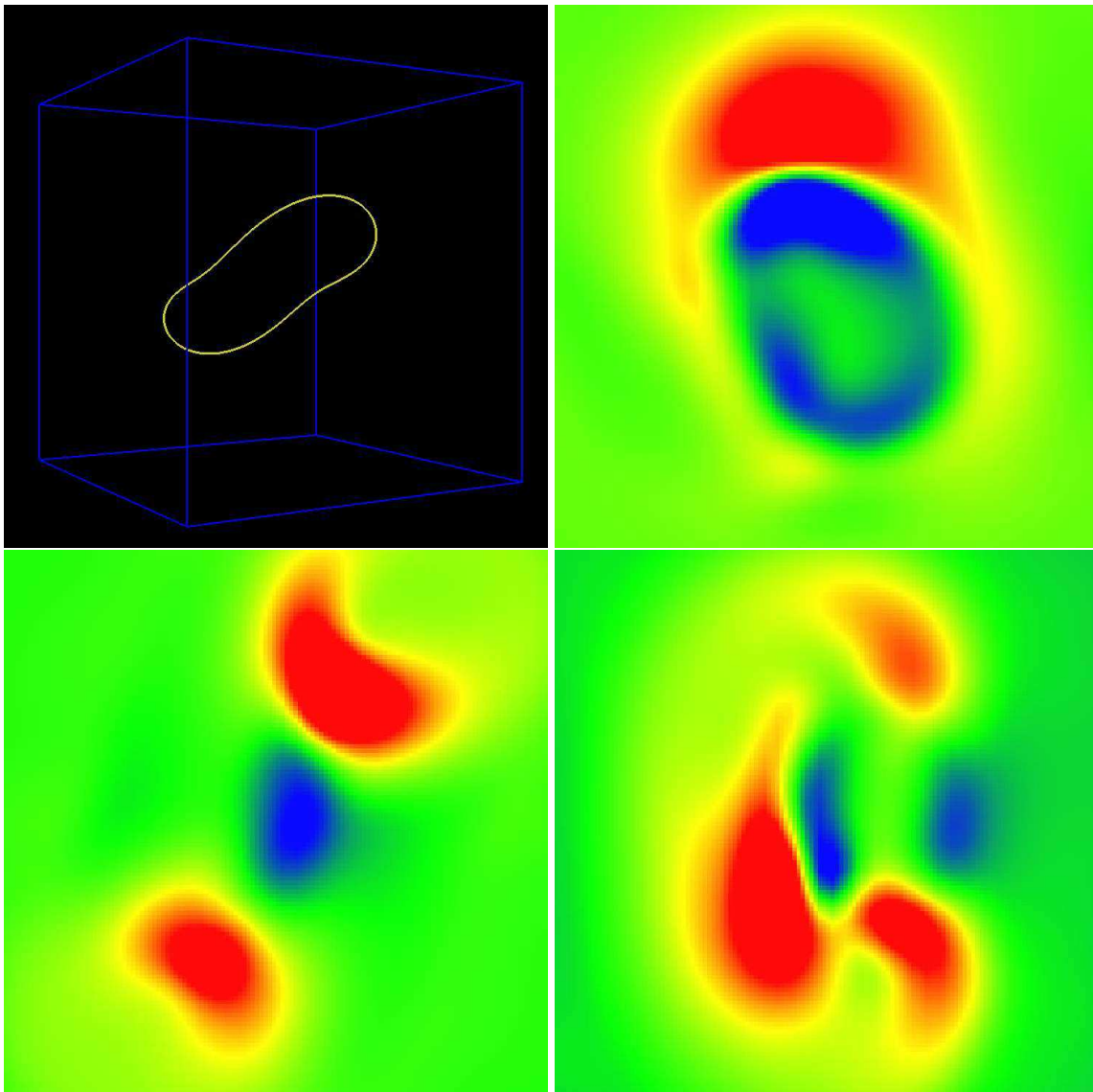


FIG. 6: CMB fluctuations seeded by a single (Kibble-Turok) loop (top-left): front view (top-right), side view (bottom-left) and top view (bottom-right).

VI. DISCUSSION

We have presented the full set of sourced evolution equations with the Boltzmann hierarchy necessary to study the gravitational effects of cosmic defects on the CMB. We have focussed attention on using cosmic string simulations as the evolving causal source terms in these equations. We have developed efficient numerical techniques for the Green's function computation of high accuracy maps from these string network simulations. We have also presented numerical tests of the full pipeline. More quantitative results from extensive supercomputer simulations will be presented in [33, 34], featuring large-angle and small-angle maps respectively.

Acknowledgements

We are grateful for useful discussions with Gareth Amery, Richard Battye, Martin Bucher, Carlos Martins and Proty Wu. ML acknowledges the support of the FCAR Fund; the Cambridge Commonwealth Trust; ORS; Peterhouse; the Canadian Centennial Scholarship Fund; and the Cambridge Philosophical Society. This work was supported by PPARC grant no. PPA/G/O/1999/00603. Simulations were performed on COSMOS, the Origin 3000 supercomputer,

owned by the UK cosmology consortium and funded by SGI/Cray Research, HEFCE and PPARC.

-
- [1] A. Vilenkin and E.P.S. Shellard, *Cosmic Strings and other Topological Defects* (Cambridge University Press, 2000).
 - [2] P. de Bernardis et al., *Nature* **404**, 955 (2000).
 - [3] S. Hanany et al., *ApJ Lett* **545**, L5 (2000).
 - [4] P. Scott et al., astro-ph/0205380.
 - [5] T. Pearson et al., astro-ph/0205388.
 - [6] F. Bouchet, P. Peter, A. Riazuelo, and M. Sakellariadou, *Phys.Rev.* **D65**, 021301 (2002).
 - [7] C. Contaldi, astro-ph/0005115.
 - [8] N. Kaiser and A. Stebbins, *Nature* **310**, 391 (1984).
 - [9] J. Gott, *ApJ* **288**, 422 (1985).
 - [10] S. Veeraghavan and A. Stebbins, *ApJ Lett* **395**, L55 (1992).
 - [11] F. Bouchet, D. Bennet, and A. Stebbins, *Nature* **335**, 410 (1988).
 - [12] U. Pen, D. Spergel, and N. Turok, *Phys.Rev.* **D49**, 692 (1994).
 - [13] D. Coulson, P. Ferreira, P. Graham, and N. Turok, *Nature* **368**, 27 (1994).
 - [14] B. Allen, R. Caldwell, E.P.S. Shellard, A. Stebbins, and S. Veeraghavan, *Phys.Rev.Lett.* **77**, 3061 (1996).
 - [15] B. Allen and E.P.S. Shellard, *Phys.Rev.Lett.* **64**, 119 (1990).
 - [16] B. Allen, R. Caldwell, S. Dodelson, L. Knox, E.P.S. Shellard, and A. Stebbins, *Phys.Rev.Lett.* **79**, 2624 (1997).
 - [17] U. Pen, U. Seljak, and N. Turok, *Phys.Rev.Lett.* **79**, 1611 (1997).
 - [18] R. Durrer, M. Kunz, and A. Melchiorri, *Phys.Rev.* **D59**, 123005 (1999).
 - [19] C. Contaldi, M. Hindmarsh, and J. Magueijo, *Phys.Rev.Lett* **82**, 679 (1999).
 - [20] A. Albrecht, R. Battye, and J. Robinson, *Phys.Rev.* **D59**, 023508 (1999).
 - [21] L. Pogosian and T. Vachaspati, *Phys. Rev.* **D60**, 083504 (1999).
 - [22] N. Simatos and L. Perivolaropoulos, *Phys.Rev.* **D63**, 025018 (2001).
 - [23] C. Ma and E. Bertschinger, *ApJ* **455**, 7 (1995).
 - [24] A. Melchiorri and N. Vittorio, in *Proceedings of the NATO Advanced Study Institute on the CBR* (1996).
 - [25] R. Sachs and A. Wolfe, *ApJ* **147**, 73 (1967).
 - [26] M. Landriau, Ph.D. thesis, University of Cambridge (2003).
 - [27] S. Seager, D. Sasselov, and D. Scott, *ApJ Lett.* **523**, L1 (1999).
 - [28] W. Press, S. Teukolsky, W. Vetterling, and B. Flannery, *Numerical Recipes in C, The Art of Scientific Computing* (Cambridge University Press, 1992), second edition ed.
 - [29] U. Aschor and L. Petzold, *Computer Methods for Ordinary Differential Equations and Differential Algebraic Equations* (Society for industrial and applied mathematics, 1998).
 - [30] S. Veeraghavan and A. Stebbins, *ApJ* **365**, 37 (1990).
 - [31] G. Amery and E.P.S. Shellard, *Phys.Rev.* **D67**, 083502 (2003), ; astro-ph/0208413.
 - [32] T. Kibble and N. Turok, *Phys.Lett.* **116B**, 141 (1982).
 - [33] M. Landriau and E.P.S. Shellard (2003), astro-ph/0302166.
 - [34] M. Landriau and E.P.S. Shellard, DAMTP report.